Appl. Math. Mech. -Engl. Ed., **44**(6), 877–896 (2023)

APPLIED MATHEMATICS AND MECHANICS (ENGLISH EDITION)

https://doi.org/10.1007/s10483-023-3008-7

A novel way for vibration control of FGM fluid-conveying pipes via NiTiNOL-steel wire rope*

Jian ZANG[1], Ronghuan XIAO[1], Yewei ZHANG[1,†], Liqun CHEN[2]

1. College of Aerospace Engineering, Shenyang Aerospace University, Shenyang 110136, China;
2. Shanghai Institute of Applied Mathematics and Mechanics, School of Mechanics and Engineering Science, Shanghai University, Shanghai 200444, China

(Received Dec. 30, 2022 / Revised Mar. 10, 2023)

Abstract In this study, a coupling model of fluid-conveying pipes made of functionally graded materials (FGMs) with NiTiNOL-steel (NiTi-ST) for vibration absorption is investigated. The vibration responses of the FGM fluid-conveying pipe with NiTi-ST are studied by the Galerkin truncation method (GTM) and harmonic balance method (HBM). The harmonic balance solutions and the numerical results are consistent. Also, the linearized stability of the structure is determined. The effects of the structure parameters on the absorption performance are also studied. The results show that the NiTi-ST is an effective means of vibration absorption. Furthermore, in studying the effect of the NiTi-ST, a closed detached response (CDR) is first observed. It is noteworthy that the CDR may dramatically change the vibration amplitude and that the parameters of the NiTi-ST may determine the emergence or disappearance of the CDR. This vibration absorption device can be extended to offer more general vibration control in engineering applications.

Key words NiTiNOL-steel (NiTi-ST), functionally graded material (FGM) fluid-conveying pipe, vibration absorption, harmonic balance method (HBM), closed detached response (CDR)

Chinese Library Classification O242
2010 Mathematics Subject Classification 74H10

1 Introduction

Fluid-conveying pipes have a variety of applications in many fields, including nuclear power plants, aerospace engineering, and oil industry[1–2]. In the past decades, vibration of fluid-conveying pipes has received widespread attention, most of which focused on natural frequencies, modes, and stability[3–4]. Flow velocity, boundary conditions, axial motion, and other factors can influence the vibration response of fluid-conveying pipes[5–8], and the vibration absorption of fluid-conveying pipes deserves additional research[9–10].

---

* Citation: ZANG, J., XIAO, R. H., ZHANG, Y. W., and CHEN, L. Q. A novel way for vibration control of FGM fluid-conveying pipes via NiTiNOL-steel wire rope. *Applied Mathematics and Mechanics* (*English Edition*), **44**(6), 877–896 (2023) https://doi.org/10.1007/s10483-023-3008-7

† Corresponding author, E-mail: zhangyewei1218@126.com

Project supported by the National Natural Science Foundation of China (Nos. 12272240 and 12022213)

With the development of material science, the functionally graded materials (FGMs) have been studied by researchers[11–12]. Compared with traditional composites, FGMs have various advantages, such as small stress concentration and improved thermal properties[13]. Therefore, FGMs have been applied to the fluid-conveying pipes design. An FGM periodic shell structure has been proposed for enhancing the stability of the shell system and solving the stress concentration problems. At the same time, the dynamic stability of spring support was evaluated[14]. When the vibration response and dynamic characteristics of FGM fluid-conveying pipes were investigated. It is found that functionally graded pipes have obviously enhanced stability compared with aluminum and steel pipes[15–17]. Therefore, the study of FGM fluid-conveying pipes has important significance for engineering applications. Su et al.[18] investigated the transient heat conduction and vibration performance of FGM fluid-conveying pipes for the pipe systems such as nuclear engineering, aviation, and energy fields. The micro-scale FGM fluid-conveying pipe was studied for the special applications in engineering[19]. Saleh and Ahmed[20] developed the FGM tubes by centrifugal casting to increase the mechanical properties and wear resistance in transport and automobile applications. Relying on the excellent performance of FGM fluid-conveying pipes, the FGM fluid-conveying pipe has a good prospect in engineering applications.

To reduce the negative effect of vibration on fluid-conveying pipes, passive vibration absorption methods have been widely adopted due to simply designed, economical, and practical properties. For example, Zhu et al.[21] illustrated the stability of an FGM fluid-conveying pipe with nonlinear elastic foundation. Ding et al.[22] proposed a quasi-zero stiffness isolator for fluid-conveying pipes, and discussed the effects on the vibration characteristics. The nonlinear attached absorber has received extensive attention as a typical representation of nonlinear passive control devices[23]. The nonlinear attached absorber has broadband absorption and high robustness[24–27], and it has been applied in vibration energy harvesters[28–31] and in many engineering structures such as beams[32–33], laminated plates[34], and pipes[35]. These passive control devices improve the system stability, and increase the vibration absorption bandwidth. Hence, they are widely used for the vibration absorption in engineering structures, but there are also obvious disadvantages such as the need for a certain installation space, a certain movement stroke, and an increase in the adhesion quality of structures. Therefore, new passive vibration absorbers are still required.

Shape memory alloys (SMAs) can provide a large reaction force and restore original shape when experiencing strain. SMAs have many excellent characteristics such as energy dissipation through hysteresis response, resistance to corrosion, high strength, and fatigue resistance[36–37]. SMA composite structures are becoming increasingly accepted in engineering applications and bring many advantages such as self-healing, improved damping, improved vibration control, and damage isolation[38]. SMAs are promising materials for passive vibration absorption. Mani and Senthilkumar[39] developed an adaptive passive dynamic damper using SMA springs to attenuate a series of excitation frequencies. Belhaq et al.[40] proposed a new type of vibration absorber based on the restoring and damping forces of NiTiNOL-steel (NiTi-ST) under bending or tension-bending coupling conditions. The characteristics of hysteresis energy dissipation caused by inter-line friction were described by the nonlinear hysteretic beam model[41]. The hysteresis beam model was illustrated with a modified Bouc-Wen mode, and the nonlinear dynamical characteristics of different configurations NiTi-ST were experimentally tested[42–43]. Brewick et al.[44] and Carboni et al.[45] established a general NiTi-ST model using data-driven methods, including polynomial basis functions and neural networks, and supplied reduced-order nonlinear models that precisely fit different data sets through naive elastic net regularization. The nonlinear characteristics of NiTi-ST can be described by the polynomial model[46]. At the present time, most researchers focus on the NiTi-ST parameter identification. The applications on nonlinear vibration control have rarely been reported, and the research on the vibration absorption of FGM fluid-conveying pipes coupled with NiTi-ST has rarely been presented.

The introduction of nonlinearity may lead to complex dynamical behavior of the system, and the dynamics of the system may show softening or hardening behavior or cause bifurcations of the system[47–48]. In addition, a special phenomenon called closed detached response (CDR) has been discovered[49–50]. The emergence and disappearance of the CDR will significantly affect system's response. Zang et al.[51–54] investigated the effects of the CDR on the vibration absorption and energy harvesting for nonlinear energy sinks or beam systems. The results showed that the effects of the CDR on structures could not be ignored, and the emergence or disappearance of the CDR would significantly affect the amplitude and energy harvesting efficiency. As far as the authors know, there is no research on discussing the CDR phenomenon of the fluid-conveying pipes coupled with NiTi-ST. It has not previously been clarified how the CDR phenomenon affects vibration absorption.

This paper presents a study of NiTi-ST coupled to an FGM fluid-conveying pipe. The paper is arranged as follows. In Section 2, the FGM fluid-conveying pipe with asymmetrical ends coupling to the NiTi-ST is described, and then a mathematical model is built. The modal functions and the natural frequency can be obtained by simplifying the system. Section 3 presents the Galerkin truncation method (GTM) to facilitate the simulation calculation. Section 4 examines the effects of the system parameters on the vibration absorption with the harmonic balance method (HBM). Section 5 draws conclusions.

2 Model of the system

2.1 Dynamic function

The fluid-conveying pipe made of vertically FGMs coupled with NiTi-ST is shown in Fig. 1. The NiTi-ST is coupled to the FGM fluid-conveying pipe and completely fixed on the fluid-conveying pipe surface. The boundary of the system is asymmetrical, the left end of the pipe is fixed, and the right end of the pipe is supported by a linear spring.

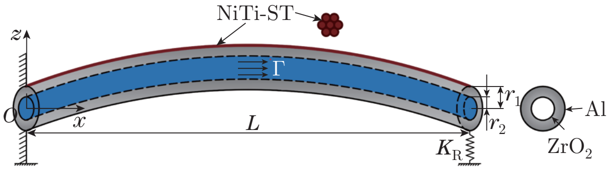

Fig. 1 FGM fluid-conveying pipe coupled with NiTi-ST (color online)

The fluid-conveying pipe is modeled as the Euler-Bernoulli beam with length L, outer radius r_1, and inner radius r_2. A_f and A_p represent the cross-sectional areas of the fluid and the pipe, respectively. The rotary inertial and shearing strains are ignored. The fluid is incompressible and non-viscous, and moves at a constant velocity Γ in the pipe. The density of the fluid is ρ_f. This paper assumes that the FGM fluid-conveying pipe is composed of ceramic and metal. The modulus of elasticity, density, and Poisson's ratio vary exponentially along the vertical direction, which can be written as

$$\begin{cases} E(r) = E_1 + (E_2 - E_1)\Big(\dfrac{r - r_1}{r_2 - r_1}\Big)^{\widehat{m}}, \\ \rho(r) = \rho_1 + (\rho_2 - \rho_1)\Big(\dfrac{r - r_1}{r_2 - r_1}\Big)^{\widehat{m}}, \\ \nu(r) = \nu_1 + (\nu_2 - \nu_1)\Big(\dfrac{r - r_1}{r_2 - r_1}\Big)^{\widehat{m}}. \end{cases} \tag{1}$$

The distribution of materials is in the radial direction, and $\widehat{m}$ ($\widehat{m} \geqslant 0$) denotes the material gradient index. Consequently, it is pure metal or ceramic for the internal surface or outside surface of the fluid-conveying pipe.

Based on the Euler-Bernoulli beam theory, the displacements at any point along the FGM fluid-conveying pipe take the following form:

$$\begin{cases} U(x,y,z,t)=u(x,t)-z\dfrac{\partial w}{\partial x}, \\ V(x,y,z,t)=0, \\ W(x,y,z,t)=w(x,t), \end{cases} \tag{2}$$

where $u(x,t)$ is the axial displacement, $w(x,t)$ is the transverse displacement, and t is time.

The kinetic energy of the FGM fluid-conveying pipe is written as

$$T=\frac{1}{2}\int_0^L m_{\mathrm{p}}((u_{,t})^2+(w_{,t})^2)\mathrm{d}x+\frac{1}{2}\int_0^L m_{\mathrm{f}}\Big(\Gamma+\frac{\mathrm{d}u}{\mathrm{d}t}\Big)^2\mathrm{d}x+\frac{1}{2}\int_0^L m_{\mathrm{f}}\Big(\frac{\mathrm{d}w}{\mathrm{d}t}\Big)^2\mathrm{d}x, \tag{3}$$

where the subscript t represents the partial derivative of time, and $\frac{\mathrm{d}(\cdot)}{\mathrm{d}t}$ stands for the first derivative with respect to time. The subscript "," indicates a partial derivative, m_{p} and m_{f} are the mass of the fluid-conveying pipe and that of the fluid per unit length, respectively. They are written as

$$m_{\mathrm{p}}=\int_{A_{\mathrm{p}}}\rho(r)\mathrm{d}A_{\mathrm{p}}=\int_0^{2\pi}\int_{r1}^{r2}\rho(r)r\mathrm{d}r\mathrm{d}\theta,\quad m_{\mathrm{f}}=\int_{A_{\mathrm{f}}}\rho_{\mathrm{f}}\mathrm{d}A_{\mathrm{f}}. \tag{4}$$

Ignoring the shear deformation and considering only one-dimensional linear elastic behavior, the strain of the FGM fluid-conveying pipe is expressed as

$$\varepsilon_z=u_{,x}-zw_{,xx}. \tag{5}$$

Hence, the strain energy is given by

$$\begin{aligned} U_{\mathrm{E}} &=\frac{1}{2}\int_{\Omega}\sigma_x\varepsilon_x\mathrm{d}\Omega+\int_0^L A_{\mathrm{f}}P(\sqrt{(\mathrm{d}x+\mathrm{d}u)^2-(\mathrm{d}w)^2}-\mathrm{d}x) \\ &=\frac{1}{2}\int_0^L(N_xu_{,x}-Mw_{,xx})\mathrm{d}x+\int_0^L A_{\mathrm{f}}P(\sqrt{(1+u_{,x})^2+(w_{,xx})^2}-1)\mathrm{d}x, \end{aligned} \tag{6}$$

where σ_x is the stress of the FGM fluid-conveying pipe, and P is the fluid pressure per unit area. N_x and M are, respectively, the axial force and the transverse bending moment. They are given by

$$N_x=\int_A\sigma_x\mathrm{d}A=A_{11}u_{,x}-B_{11}w_{,xx},\quad M=\int_A\sigma_xz\mathrm{d}A=B_{11}u_{,x}-D_{11}w_{,xx}, \tag{7}$$

where

$$(A_{11},B_{11},D_{11})=\int_A Q(r)(1,r,r^2)\mathrm{d}A,\quad Q(r)=\frac{E(r)}{1-\nu(r)}. \tag{8}$$

Furthermore, the virtual work done by the reaction force of the linear spring and uniformly distributed harmonic excitation $q(x,t)$ is given as

$$\delta W_{\mathrm{f}}=\int_0^L f\cos(\omega t)\delta w\mathrm{d}x+\int_0^L\frac{1}{2}K_{\mathrm{R}}w(L,t)\delta w(L,t)\mathrm{d}x, \tag{9}$$

where K_{R} is the stiffness of the vertical support springs, f is the amplitude of harmonic excitation, and ω is the frequency of external excitation. The restoring and damping force f_{st} of the NiTi-ST can be written as

$$f_{\mathrm{st}} = (1-r)k_{\mathrm{c}}w^3 + r(k_{\mathrm{e}}w + z_h). \tag{10}$$

The force f_{st} is in connection with the displacement of the FGM fluid-conveying pipe. r, k_{c}, and k_{e} are the experimental parameters. The experimental model is an in-house-built rheological device designed by Carboni et al.[42]. This experimental model is made of assemblies of custom-made nickel titanium-naval ordnance laboratory strands wires and steel wire ropes. Different configurations of NiTi-ST are placed in the rheological device. According to interline friction, phase transition, and geometric nonlinearities, the material behavior can be obtained[44]. Through the modified Bouc-Wen model, the hysteresis damping force z_h can be written as[41]

$$\begin{cases} \dot{z}_h = (k_{\mathrm{d}}h(x) - (\widehat{\gamma} + \beta\,\mathrm{sgn}(z_h\dot{w}))|z_h|^n)\dot{w}, \\ h(x) = 1 - \xi \mathrm{e}^{-\frac{w^2}{w_{\mathrm{c}}}}, \end{cases} \tag{11}$$

where $k_{\mathrm{d}}, \widehat{\gamma}, \beta, n, \xi$, and w_{c} are parameters related to the materials. To keep the expression for the force f_{st} as simple as possible, it is taken to have a polynomial form. According to the polynomial fitting method, the polynomial function basis has five items, and can be written as

$$f_{\mathrm{st}} = k_1 w + k_3 w^3 + c_1\dot{w} + r_{21}w^2\dot{w} - r_{12}w\dot{w}^2, \tag{12}$$

where k_1 and k_3 are the stiffness coefficients, c_1, r_{21}, and r_{12} are the damping coefficients, and "." indicates time derivative. There are three different configurations of NiTi-ST considered in this paper. Here, we focus on the S1a configuration. The polynomial fitting results are listed in Table 1[55].

Table 1 Parameters of restoring and damping force model

Configuration	$k_1/(\mathrm{N\cdot m^{-1}})$	$k_3/(\mathrm{N\cdot m^{-3}})$	$c_1/(\mathrm{N\cdot s\cdot m^{-1}})$	$r_{12}/(\mathrm{N\cdot s^2\cdot m^{-3}})$	$r_{21}/(\mathrm{N\cdot s\cdot m^{-3}})$	R-square
S1a	–	4.097×10^8	122.4	6.515×10^4	1.699×10^6	0.998 3
S2a	5 966	–	52.09	9 876	1.259×10^5	0.998 6
S2b	4 523	–	16.49	2 608	1.077×10^5	0.996 3

The virtual work done by the restoring and damping force can therefore be given by

$$\delta W_{\mathrm{st}} = \int_0^L -\chi f_{\mathrm{st}}\delta w\mathrm{d}x, \tag{13}$$

where χ is a parameter modifying the restoring and damping force. Considering only the transverse motion, according to the Hamilton theory and Eqs. (3), (6), (9), and (12), one gets

$$\delta\int_0^L (T - U_{\mathrm{E}})\mathrm{d}t + \int_{t_1}^{t_2}(\delta W_{\mathrm{f}} + \delta W_{\mathrm{st}})\mathrm{d}t = 0. \tag{14}$$

The governing equation of the system is found to be

$$\begin{aligned} &(m_{\mathrm{p}} + m_{\mathrm{f}})w_{,tt} + (m_{\mathrm{f}}\Gamma^2 - A_{\mathrm{f}}P)w_{,xx} + 2m_{\mathrm{f}}\Gamma w_{,xt} + D_{11}w_{,xxxx} - f\cos(wt) \\ &+ \chi(k_1w + k_3w^3 + c_1\dot{w} + r_{21}w^2\dot{w} - r_{12}w\dot{w}^2) = 0. \end{aligned} \tag{15}$$

The boundary conditions are given by

$$\begin{cases} w(0,t)=0, \quad w_{,x}(0,t)=0, \quad D_{11}w_{,xx}(L,t)=0, \\ (m_{\mathrm{f}}\Gamma^2 - A_{\mathrm{f}}P)w_{,x}(L,t) + D_{11}w_{,xxx}(L,t) - K_{\mathrm{R}}w(L,t)=0. \end{cases} \tag{16}$$

The dimensionless parameters and variables are introduced as follows:

$$\begin{cases} \overline{w}=\dfrac{w}{L}, \quad \overline{x}=\dfrac{x}{L}, \quad \overline{t}=\dfrac{t}{L^2}\sqrt{\dfrac{E_0I_{\mathrm{p}}}{\rho_{p_0}A_{\mathrm{p}}+\rho_{\mathrm{f}}A_{\mathrm{f}}}}, \quad \overline{m}_{\mathrm{p}}=\dfrac{m_{\mathrm{p}}}{\rho_{p_0}A_{\mathrm{p}}+\rho_{\mathrm{f}}A_{\mathrm{f}}}, \\ \overline{m}_{\mathrm{f}}=\dfrac{m_{\mathrm{f}}}{\rho_{p_0}A_{\mathrm{p}}+\rho_{\mathrm{f}}A_{\mathrm{f}}}, \quad \gamma=\Gamma L\sqrt{\dfrac{m_{\mathrm{f}}}{E_0I_{\mathrm{p}}}}, \quad \Lambda=\dfrac{A_{\mathrm{f}}PL^2}{E_0I_{\mathrm{p}}}, \quad \overline{f}=\dfrac{fL^2}{E_0I_{\mathrm{p}}}, \\ \overline{\omega}=\omega L\sqrt{\dfrac{\rho_{p_0}A_{\mathrm{p}}+\rho_{\mathrm{f}}A_{\mathrm{f}}}{E_0I_{\mathrm{p}}}}, \quad \overline{k}_{\mathrm{R}}=\dfrac{K_{\mathrm{R}}L^3}{E_0I_{\mathrm{p}}}, \quad d_{11}=\dfrac{D_{11}}{E_0I_{\mathrm{p}}}, \\ \overline{k}_1=\dfrac{k_1L^4}{E_0I_{\mathrm{p}}}, \quad \overline{k}_3=\dfrac{k_3L^4}{E_0I_{\mathrm{p}}}, \quad \overline{c}_1=c_1L^2\sqrt{\dfrac{1}{E_0I_{\mathrm{p}}(\rho_{p_0}A_{\mathrm{p}}+\rho_{\mathrm{f}}A_{\mathrm{f}})}}, \\ \overline{r}_{21}=r_{21}L^3\sqrt{\dfrac{1}{E_0I_{\mathrm{p}}(\rho_{p_0}A_{\mathrm{p}}+\rho_{\mathrm{f}}A_{\mathrm{f}})}}, \quad \overline{r}_{12}=r_{21}L\sqrt{\dfrac{1}{E_0I_{\mathrm{p}}(\rho_{p_0}A_{\mathrm{p}}+\rho_{\mathrm{f}}A_{\mathrm{f}})}}. \end{cases} \tag{17}$$

The dimensionless governing equation and relative boundary conditions of the system can be given as

$$\begin{aligned} &(\overline{m}_{\mathrm{p}}+\overline{m}_{\mathrm{f}})\overline{w}_{,\overline{tt}} + (\gamma^2-\Lambda)\overline{w}_{,\overline{xx}} + 2\sqrt{\overline{m}_{\mathrm{f}}}\gamma\overline{w}_{,\overline{xt}} + d_{11}\overline{w}_{\overline{xxxx}} - \overline{f}\cos(\overline{\omega}\overline{t}) \\ &+\chi(\overline{k}_1\overline{w} + \overline{k}_3\overline{w}^3 + \overline{c}_1\dot{\overline{w}} + \overline{r}_{21}\overline{w}^2\dot{\overline{w}} - \overline{r}_{12}\overline{w}\dot{\overline{w}}^2)=0, \end{aligned} \tag{18}$$

$$\begin{cases} \overline{w}(0,\overline{t})=0, \quad \overline{w}_{,\overline{x}}(0,\overline{t})=0, \quad d_{11}w_{,\overline{xx}}(1,\overline{t})=0, \\ (\gamma^2-\Lambda)\overline{w}_{,\overline{x}}(1,\overline{t}) + d_{11}w_{,\overline{xxx}}(1,\overline{t}) - \overline{k}_{\mathrm{R}}\overline{w}(1,\overline{t})=0, \end{cases} \tag{19}$$

where ρ_{p_0} and E_0 are, respectively, the density and the modulus of elasticity of the fluid-conveying pipe made completely of metal.

2.2 Natural frequency and modal function

The linear dimensionless governing equation of the FGM fluid-conveying pipe can be written as

$$(\overline{m}_{\mathrm{p}}+\overline{m}_{\mathrm{f}})\overline{w}_{,\overline{tt}} + (\gamma^2-\Lambda)\overline{w}_{,\overline{xx}} + 2\sqrt{\overline{m}_{\mathrm{f}}}\gamma\overline{w}_{,\overline{xt}} + d_{11}\overline{w}_{,\overline{xxxx}}=0. \tag{20}$$

The displacement of the FGM fluid-conveying pipe can be assumed to be

$$\overline{w}(\overline{x},\overline{t})=\phi(\overline{x})\mathrm{e}^{\mathrm{i}\overline{\omega}\overline{t}}, \tag{21}$$

$$\phi(\overline{x})=C_1\mathrm{e}^{\mathrm{i}\beta_1\overline{x}} + C_2\mathrm{e}^{\mathrm{i}\beta_2\overline{x}} + C_3\mathrm{e}^{\mathrm{i}\beta_3\overline{x}} + C_4\mathrm{e}^{\mathrm{i}\beta_4\overline{x}}, \tag{22}$$

where $\mathrm{e}^{\mathrm{i}\overline{\omega}\overline{t}}$ and $\phi(\overline{x})$ are the generalized coordinate and modal functions of the system, respectively, and β_j $(j=1,2,3,4)$ are eigenvalues. To obtain an expression relating frequency and eigenvalues, Eqs. (21) and (22) are substituted into Eq. (20),

$$d_{11}\beta_j^4 - (\gamma^2-\Lambda)\beta_j^2 - 2\sqrt{\overline{m}_{\mathrm{f}}}\gamma\beta_j\overline{\omega} - (\overline{m}_{\mathrm{p}}+\overline{m}_{\mathrm{f}})\overline{\omega}^2=0. \tag{23}$$

The coefficients C_1, C_2, C_3, and C_4 can be found by substituting Eq. (22) into the governing equation with dimensionless boundary conditions, which are found to be

$$\begin{cases} C_1 + C_2 + C_3 + C_4 = 0, \\ \mathrm{i}C_1\beta_1 + \mathrm{i}C_2\beta_2 + \mathrm{i}C_3\beta_3 + \mathrm{i}C_4\beta_4 = 0, \\ -C_1\beta_1^2\mathrm{e}^{\mathrm{i}\beta_1} - C_2\beta_2^2\mathrm{e}^{\mathrm{i}\beta_2} - C_3\beta_3^2\mathrm{e}^{\mathrm{i}\beta_3} - C_4\beta_4^2\mathrm{e}^{\mathrm{i}\beta_4} = 0, \\ (\gamma^2 - \Lambda)(\mathrm{i}C_1\beta_1\mathrm{e}^{\mathrm{i}\beta_1} + \mathrm{i}C_2\beta_2\mathrm{e}^{\mathrm{i}\beta_2} + \mathrm{i}C_3\beta_3\mathrm{e}^{\mathrm{i}\beta_3} + \mathrm{i}C_4\beta_4\mathrm{e}^{\mathrm{i}\beta_4}) \\ +d_{11}(-\mathrm{i}C_1\beta_1^3\mathrm{e}^{\mathrm{i}\beta_1} - \mathrm{i}C_2\beta_2^3\mathrm{e}^{\mathrm{i}\beta_2} - \mathrm{i}C_3\beta_2^3\mathrm{e}^{\mathrm{i}\beta_3} - \mathrm{i}C_4\beta_4^3\mathrm{e}^{\mathrm{i}\beta_4}) \\ +\overline{k}_{\mathrm{R}}(C_1\mathrm{e}^{\mathrm{i}\beta_1} + C_2\mathrm{e}^{\mathrm{i}\beta_2} + C_3\mathrm{e}^{\mathrm{i}\beta_3} + C_4\mathrm{e}^{\mathrm{i}\beta_4}) = 0. \end{cases} \tag{24}$$

According to Eq. (24), the coefficients C_1, C_2, C_3, and C_4 are found to be

$$\begin{cases} C_1 = 1, \\ C_2 = \dfrac{C_1(\mathrm{e}^{\mathrm{i}\beta_3}\beta_1\beta_3^2 - \mathrm{e}^{\mathrm{i}\beta_3}\beta_4\beta_3^2 - \mathrm{e}^{\mathrm{i}\beta_4}\beta_1\beta_4^2 + \mathrm{e}^{\mathrm{i}\beta_4}\beta_3\beta_4^2 - \mathrm{e}^{\mathrm{i}\beta_1}\beta_1^2\beta_3 + \mathrm{e}^{\mathrm{i}\beta_1}\beta_1^2\beta_4}{\mathrm{e}^{\mathrm{i}\beta_2}\beta_2\beta_2^2 - \mathrm{e}^{\mathrm{i}\beta_2}\beta_4\beta_2^2 - \mathrm{e}^{\mathrm{i}\beta_3}\beta_2\beta_3^2 + \mathrm{e}^{\mathrm{i}\beta_3}\beta_4\beta_3^2 + \mathrm{e}^{\mathrm{i}\beta_4}\beta_2\beta_4^2 - \mathrm{e}^{\mathrm{i}\beta_4}\beta_3\beta_4^2}, \\ C_3 = -\dfrac{C_1(\mathrm{e}^{\mathrm{i}\beta_2}\beta_1\beta_2^2 - \mathrm{e}^{\mathrm{i}\beta_2}\beta_4\beta_2^2 - \mathrm{e}^{\mathrm{i}\beta_4}\beta_1\beta_4^2 + \mathrm{e}^{\mathrm{i}\beta_4}\beta_2\beta_4^2 - \mathrm{e}^{\mathrm{i}\beta_1}\beta_1^2\beta_2 + \mathrm{e}^{\mathrm{i}\beta_1}\beta_1^2\beta_4}{\mathrm{e}^{\mathrm{i}\beta_2}\beta_3\beta_2^2 - \mathrm{e}^{\mathrm{i}\beta_2}\beta_4\beta_2^2 - \mathrm{e}^{\mathrm{i}\beta_3}\beta_2\beta_3^2 + \mathrm{e}^{\mathrm{i}\beta_3}\beta_4\beta_3^2 + \mathrm{e}^{\mathrm{i}\beta_4}\beta_2\beta_4^2 - \mathrm{e}^{\mathrm{i}\beta_4}\beta_3\beta_4^2}, \\ C_4 = -\dfrac{C_1(\mathrm{e}^{\mathrm{i}\beta_2}\beta_1\beta_2^2 - \mathrm{e}^{\mathrm{i}\beta_2}\beta_3\beta_2^2 - \mathrm{e}^{\mathrm{i}\beta_3}\beta_1\beta_3^2 + \mathrm{e}^{\mathrm{i}\beta_3}\beta_2\beta_3^2 - \mathrm{e}^{\mathrm{i}\beta_1}\beta_1^2\beta_2 + \mathrm{e}^{\mathrm{i}\beta_1}\beta_1^2\beta_3}{\mathrm{e}^{\mathrm{i}\beta_2}\beta_3\beta_2^2 - \mathrm{e}^{\mathrm{i}\beta_2}\beta_4\beta_2^2 - \mathrm{e}^{\mathrm{i}\beta_3}\beta_2\beta_3^2 + \mathrm{e}^{\mathrm{i}\beta_3}\beta_4\beta_3^2 + \mathrm{e}^{\mathrm{i}\beta_4}\beta_2\beta_4^2 - \mathrm{e}^{\mathrm{i}\beta_4}\beta_3\beta_4^2}. \end{cases} \tag{25}$$

From Eqs. (23), (24), and (25), the eigenvalues and natural frequencies of the corresponding linear equations can be obtained by numerical methods. The parameters of the FGM fluid-conveying pipe are provided in Table 2.

Table 2 Parameter values of the FGM fluid-conveying pipe

Item	Notation	Value
Outer radius	r_1	0.2 m
Inner radius	r_2	0.016 m
Young's modulus	E_1	70 GPa
	E_2	151 GPa
Density of fluid	ρ_{f}	1 000 kg·m^{-3}
Density of pipe	ρ_1	2 700 kg·m^{-3}
	ρ_2	3 000 kg·m^{-3}
Length of pipe	L	1 m
Stiffness of support spring	K_{R}	30 000 N·m^{-1}
Gradient index	$\widehat{m}$	1

Figure 2 shows the effects of the fluid velocity on the natural frequency. In general, the flow velocity will affect the first four natural frequencies, which vary in a small range as the fluid velocity changes. The natural frequencies decrease with the increasing fluid velocity. Figure 3 shows how the first four modal functions depend on the linear supporting spring stiffness. Since the boundary conditions of the structure are asymmetrical, the vibration mode of the FGM fluid-conveying pipe is asymmetrical. The linear supporting spring stiffness has an obvious influence

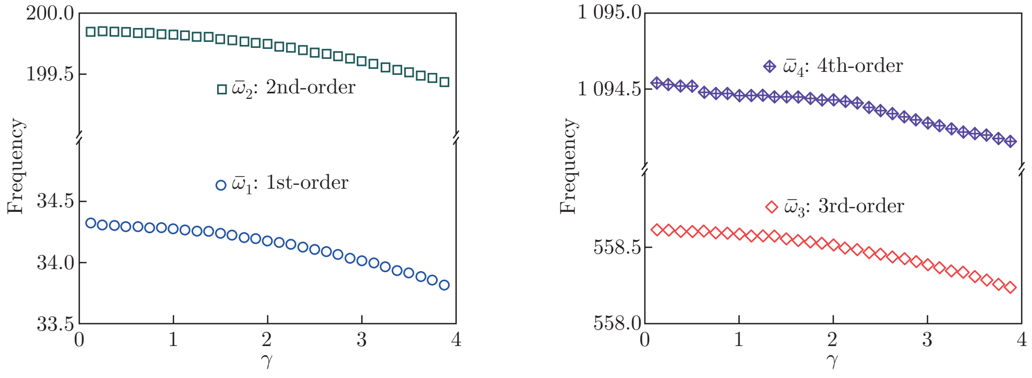

(a) (b)

Fig. 2 Effects of the fluid velocity on the natural frequency when $\overline{k}_{\mathrm{R}} = 92.7$: (a) the 1st-order and 2nd-order; (b) the 3rd-order and 4th-order (color online)

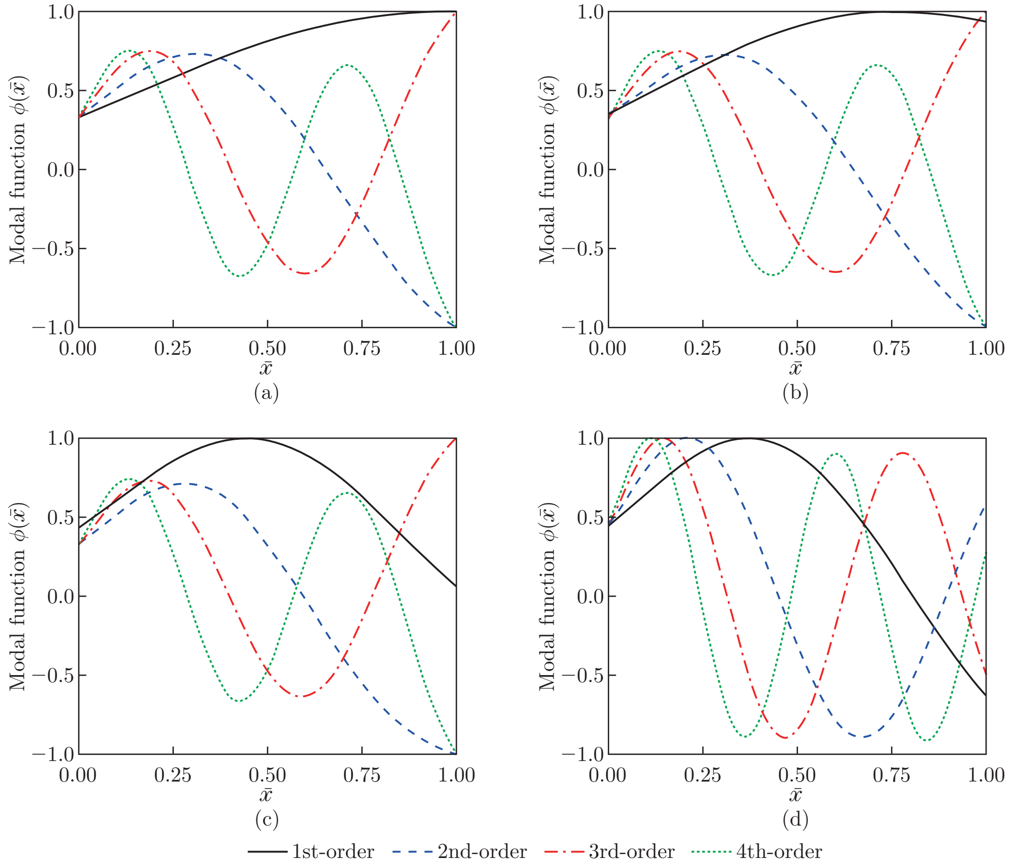

Fig. 3 Modal functions of the FGM fluid-conveying pipe when $\gamma = 1.25$: (a) $\overline{k}_{\mathrm{R}} = 9.27 \times 10^1$; (b) $\overline{k}_{\mathrm{R}} = 9.27 \times 10^2$; (c) $\overline{k}_{\mathrm{R}} = 9.27 \times 10^3$; (d) $\overline{k}_{\mathrm{R}} = 9.27 \times 10^5$ (color online)

on the first mode of the vibration modal functions. For small support stiffness, the mode change of the structure is slight, but when the support stiffness increases significantly, the mode of the structure undergoes a larger change. It is obvious from the curve of the modal function that the response of the right end changes the most significantly. The right end of the structure is the most sensitive.

3 Numerical analysis for the system

In order to facilitate the simulation calculation, the partial differential-integral equation of dynamic motion needs to be processed and transformed into an ordinary differential equation by using the GTM[53].

By neglecting the effects of the external excitation term, the damping term, and the fluid velocity, the free linear vibration and boundary conditions are given by

$$(\overline{m}_{\mathrm{p}}+\overline{m}_{\mathrm{f}})\overline{w}_{,\overline{tt}}-\Lambda\overline{w}_{,\overline{xx}}+d_{11}\overline{w}_{,\overline{xxxx}}=0, \tag{26}$$

$$\begin{cases}\overline{w}(0,\overline{t})=0, \quad \overline{w}_{,\overline{x}}(0,\overline{t})=0, \quad d_{11}\overline{w}_{,\overline{xx}}(1,\overline{t})=0,\\ d_{11}\overline{w}_{,\overline{xxx}}(1,\overline{t})-\overline{k}_{\mathrm{R}}\overline{w}(1,\overline{t})=0.\end{cases} \tag{27}$$

The free vibration displacement can be defined as

$$\overline{w}(\overline{x},\overline{t})=\varphi(\overline{x})q(\overline{t}), \tag{28}$$

where $q\overline{t}$ and $\varphi(\overline{x})$ are, respectively, the generalized coordinate and the modal function of the system. The free vibration mode function can be taken to be

$$\varphi(\overline{x})=C_{s1}\cos(\beta\overline{x})+C_{s2}\sin(\beta\overline{x})+C_{s3}\cosh(\beta\overline{x})+C_{s4}\sinh(\beta\overline{x}). \tag{29}$$

The eigenvalue β and coefficients C_{s1}, C_{s2}, C_{s3}, and C_{s4} can be determined by substituting the following equation into Eqs. (28) and (29):

$$\begin{cases}C_{s2}=(C_{s1}((d_{11}\sin(\beta)\beta^3-2\overline{k}_{\mathrm{R}}2\cos(\beta))\cosh(\beta)+\cos(\beta)\sinh(\beta)\beta^3d_{11})\\ \qquad -d_{11}\beta^3\cos(\beta)\cosh(\beta))/(d_{11}\cos(\beta)\beta^3+2\overline{k}_{\mathrm{R}}\sin(\beta)\cosh(\beta)\\ \qquad -d_{11}\beta^3\sin(\beta)\sinh(\beta)+\beta^3d_{11}),\\ C_{s3}=-(C_{s1}(-\sin(\beta)\sinh(\beta)\beta^3d_{11}-\cos(\beta)\cosh(\beta)\beta^3d_{11}-\beta^3d_{11}\\ \qquad +2\cos(\beta)\sinh(\beta)\overline{k}_{\mathrm{R}}))/(-\sin(\beta)\sinh(\beta)\beta^3d_{11}+\cos(\beta)\cosh(\beta)\beta^3d_{11}\\ \qquad +\beta^3d_{11}+2\sin(\beta)\cosh(\beta)\overline{k}_{\mathrm{R}}),\\ C_{s4}=(C_{s1}(\sin(\beta)\cos(\beta)\beta^3d_{11}+\cos(\beta)\sinh(\beta)\beta^3d_{11}-2\cos(\beta)\cosh(\beta)\overline{k}_{\mathrm{R}}))\\ \qquad /(\sin(\beta)\sinh(\beta)\beta^3d_{11}+\cos(\beta)\cosh(\beta)\beta^3d_{11}+\beta^3d_{11}+2\sin(\beta)\cosh(\beta)\overline{k}_{\mathrm{R}}).\end{cases} \tag{30}$$

Based on the obtained free vibration modal function, it is assumed that the displacement can be written as

$$\overline{w}(\overline{x},\overline{t})=\sum_{i=1}^{n}\varphi_i(\overline{x})q_i(\overline{t}), \tag{31}$$

where n stands for the Galerkin truncation term, $q_i(\overline{t})$ is the generalized coordinate, and $\varphi_i(\overline{x})$ is the free vibration modal function. By substituting Eq. (31) into the dimensionless governing equation of the system, the GTM process can be expressed as follows:

$$\begin{aligned}&(\overline{m}_{\mathrm{p}}+\overline{m}_{\mathrm{f}})\int_0^1\sum_{i=1}^{n}\varphi_i(\overline{x})\ddot{q}_i(\overline{t})\varphi_s(\overline{x})\mathrm{d}\overline{x}+(\gamma^2-\Lambda)\int_0^1\sum_{i=1}^{n}\varphi_i''(\overline{x})q_i(\overline{t})\varphi_s(\overline{x})\mathrm{d}\overline{x}\\&+2\sqrt{\overline{m}_{\mathrm{f}}}\gamma\int_0^1\sum_{i=1}^{n}\varphi_i'(\overline{x})\dot{q}_i(\overline{t})\varphi_s(\overline{x})\mathrm{d}\overline{x}+d_{11}\int_0^1\sum_{i=1}^{n}\varphi_i^{(4)}(\overline{x})q_i(\overline{t})\varphi_s(\overline{x})\mathrm{d}\overline{x}-\overline{f}\int_0^1\varphi_s(\overline{x})\mathrm{d}\overline{x}\\&+\chi\Big(\overline{k}_1\int_0^1\sum_{i=1}^{n}\varphi_i(\overline{x})q_i(\overline{t})\varphi_s(\overline{x})\mathrm{d}\overline{x}+\overline{\overline{k}}_3\int_0^1\Big(\sum_{i=1}^{n}\varphi_i(\overline{x})q_i(\overline{t})\Big)^3\varphi_s(\overline{x})\mathrm{d}\overline{x}\\&+\overline{c}_1\int_0^1\sum_{i=1}^{n}\varphi_i(\overline{x})\dot{q}_i(\overline{t})\varphi_s(\overline{x})\mathrm{d}\overline{x}+\overline{r}_{21}\int_0^1\Big(\sum_{i=1}^{n}\varphi_i(\overline{x})q_i(\overline{t})\Big)^2\Big(\sum_{i=1}^{n}\varphi_i(\overline{x})\dot{q}_i(\overline{t})\Big)\varphi_s(\overline{x})\mathrm{d}\overline{x}\\&-\overline{r}_{12}\int_0^1\Big(\sum_{i=1}^{n}\varphi_i(\overline{x})q_i(\overline{t})\Big)\Big(\sum_{i=1}^{n}\varphi_i(\overline{x})\dot{q}_i(\overline{t})\Big)^2\varphi_s\mathrm{d}\overline{x}\Big)\end{aligned}\tag{32}$$

with the weight function $\varphi_s(\overline{x})$ being the same as the free vibration modal function. Equation (32) can be simplified as

$$\begin{cases}G_{1,i}\ddot{q}_i(\overline{t})+G_{2,i}\dot{q}_i(\overline{t})+G_{3,i}q_i(\overline{t})-\overline{f}D_{4,i}\\\quad+\displaystyle\int_0^1\overline{f}\Big(\sum_{i=1}^{n}\varphi_i(\overline{x})q_i(\overline{t}),\sum_{i=1}^{n}\varphi_i(\overline{x})\dot{q}_i(\overline{t})\Big)\varphi_s(\overline{x})\mathrm{d}\overline{x}=0,\\G_{1,i}=(\overline{m}_{\mathrm{p}}+\overline{m}_{\mathrm{f}})\displaystyle\int_0^1\sum_{i=1}^{n}\varphi_i(\overline{x})\varphi_s(\overline{x})\mathrm{d}\overline{x},\\G_{2,i}=2\sqrt{\overline{m}_{\mathrm{f}}}\gamma\displaystyle\int_0^1\sum_{i=1}^{n}\varphi_i'(\overline{x})\varphi_s(\overline{x})\mathrm{d}\overline{x},\\G_{3,i}=(\gamma^2-\Lambda)\displaystyle\int_0^1\sum_{i=1}^{n}\varphi_i''(\overline{x})\varphi_s(\overline{x})\mathrm{d}\overline{x}+d_{11}\displaystyle\int_0^1\sum_{i=1}^{n}\varphi_i^{(4)}(\overline{x})\varphi_s(\overline{x})\mathrm{d}\overline{x},\\G_{4,i}=\displaystyle\int_0^1\varphi_s(\overline{x})\mathrm{d}\overline{x}.\end{cases}\tag{33}$$

Figure 4 shows the frequency history of the system for Galerkin truncations of different orders. As shown in Fig. 4, the GTM is stable and convergent. The numerical results of four-term and six-term GTMs are extremely consistent. Accordingly, the four-term GTM is used, and the results show sufficient calculational accuracy.

Figure 5(a) shows the first four orders of time-domain displacement for the FGM fluid-conveying pipe. Obviously, the differences in response for the first four natural frequencies are quite significant, with the first response being the largest. Figure 5(b) shows the corresponding displacements of the first four orders in the frequency domain. It is evident that the displacement of the first-order response is the greatest. Compared with the second, third, and fourth orders, the corresponding displacement of the first order is at least greater than one order of magnitude. This paper therefore focuses mainly on the first-order vibration response.

4 Analytical solution for the system

An analytical solution of the system is obtained by using the HBM[52]. The harmonic solution of the non-dimension coordinate is taken to be

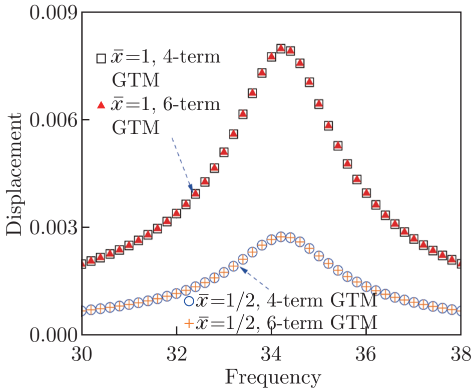

Fig. 4 Comparisons of results for different numbers of GTM terms when $\overline{k}_{\rm R} = 92.7$, $\gamma = 1.25$, and $\overline{f} = 1.5$ (color online)

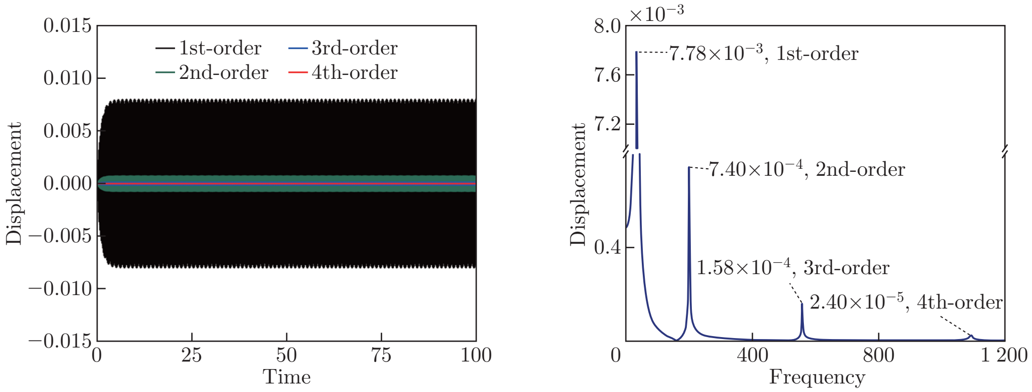

(a) (b)

Fig. 5 (a) Time-domain displacements and (b) frequency-domain displacements obtained by the 4-term GTM when $\overline{k}_{\rm R} = 92.7$, $\gamma = 1.25$, and $\overline{x} = 1$ (color online)

$$\begin{cases} q_i(\overline{t}) = \widehat{A}_{i,0} + \displaystyle\sum_{j=1}^{\dot{m}} a_{i,j}\cos(j\overline{\omega}\overline{t}) + \sum_{j=1}^{\dot{m}} b_{i,j}\sin(j\overline{\omega}\overline{t}), \\ \dot{q}_i(\overline{t}) = -\displaystyle\sum_{j=1}^{\dot{m}} a_{i,j}j\overline{\omega}\sin(j\overline{\omega}\overline{t}) + \sum_{j=1}^{\dot{m}} b_{i,j}j\overline{\omega}\cos(j\overline{\omega}\overline{t}), \\ \ddot{q}_i(\overline{t}) = -\displaystyle\sum_{j=1}^{\dot{m}} a_{i,j}j^2\overline{\omega}^2\cos(j\overline{\omega}\overline{t}) - \sum_{j=1}^{\dot{m}} b_{i,j}j^2\overline{\omega}^2\sin(j\overline{\omega}\overline{t}), \end{cases} \tag{34}$$

where j is the harmonic order. $\widehat{A}_{i,0}$ are constant terms. $a_{i,j}$ and $b_{i,j}$ are the coefficients of the cosine and sine terms, respectively.

Figure 6(a) shows the comparison of the first, third, and fifth orders of the HBM. The analytical results of the third order and fifth order are exactly comparable, while the analytical results of the first order show some deviations. Consequently, the third order is adopted in further investigations. Figure 6(b) compares the analytical solutions of the symmetrical and asymmetrical HBMs. The responses of the symmetrical and asymmetrical HBMs match accurately. This means that the constant term $\widehat{A}_{i,0}$ and the even-order harmonics in the HBM have no substantial effects on the calculated results.

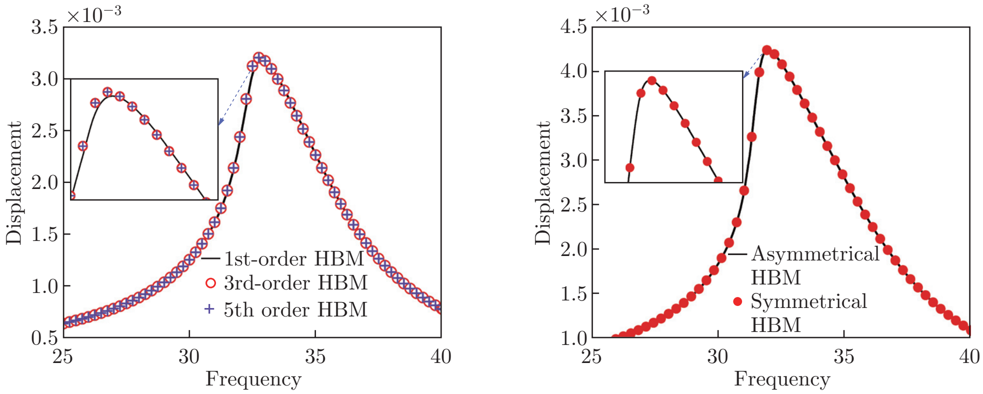

(a) (b)

Fig. 6 Comparisons of (a) different order harmonic solutions under $\overline{f} = 0.5$ and (b) asymmetrical and symmetrical HBMs under $\overline{f} = 0.7$ when $\overline{k}_{\mathrm{R}} = 92.7$, $\gamma = 1.25$, and $\overline{x} = 1$ (color online)

Figure 7 shows that the analytical solution and numerical solution are quite close. The calculation of the 3rd-order symmetrical HBM is sufficiently accurate. This verifies that the method we use is reliable and that the solution can be trusted. Hence, the remaining research reported in this paper uses the 3rd-order symmetrical HBM.

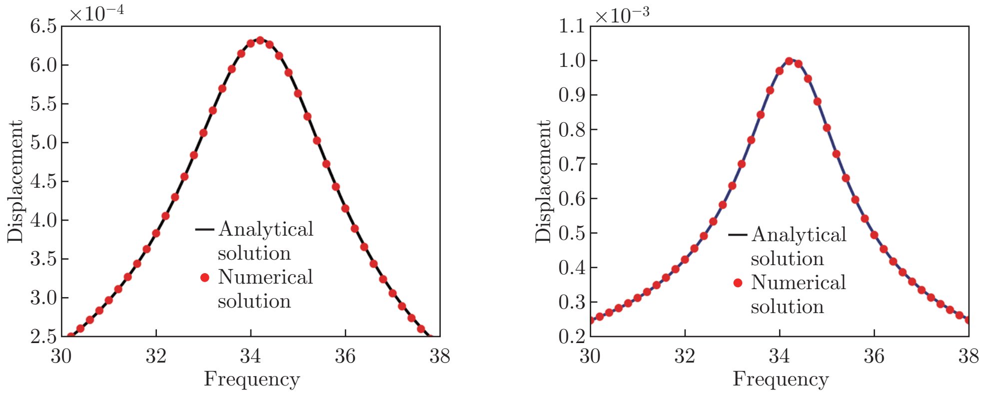

(a) (b)

Fig. 7 Comparisons of the displacements of the system obtained by analytical (3rd-order symmetrical HBM) and numerical (4-term GTM) methods (a) with and (b) without NiTi-ST when $\overline{k}_{\mathrm{R}} = 92.7$, $\gamma = 1.25$, and $\overline{x} = 1$ (color online)

The displacement responses along the FGM fluid-conveying pipe with NiTi-ST are shown in Figs. 8(a), 8(b), and 8(c). The response is measured at positions $L/2$ and L on the FGM fluid-conveying pipe. The results indicate that the amplitudes of vibration at the main resonance peaks located at $L/2$ and L are reduced by 36.04% and 36.60%, respectively. The amplitude at the right end is significantly larger than that at the midpoint. Figure 8(c) illustrates that vibration can be absorbed along the pipe. Therefore, NiTi-ST can successfully reduce the displacement of system's response, and it can provide approximate vibration absorption along the FGM fluid-conveying pipe. Hence, the vibration absorption of the NiTi-ST can be successfully applied in the FGM fluid-conveying pipe system. In Fig. 9, the effect of flow velocity on the effectiveness of the vibration absorption of the structure is shown. The results indicate that the displacement amplitude decreases with an increase in the flow velocity. As the fluid velocity increases from

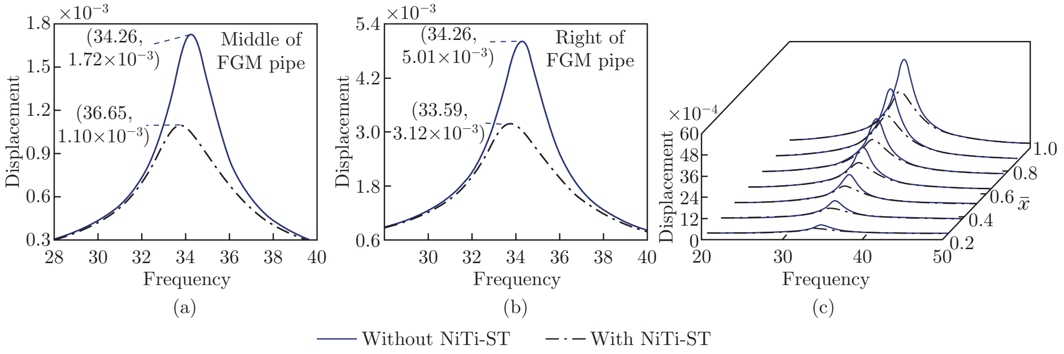

Fig. 8 Displacement along the FGM fluid-conveying pipe with NiTi-ST when $\overline{k}_{\mathrm{R}} = 92.7$, $\gamma = 1.25$, $\overline{f} = 0.5$, and (a) $\overline{x} = 1/2$ or (b) $\overline{x} = 1$. (c) Displacement changing with $\overline{x}$ (color online)

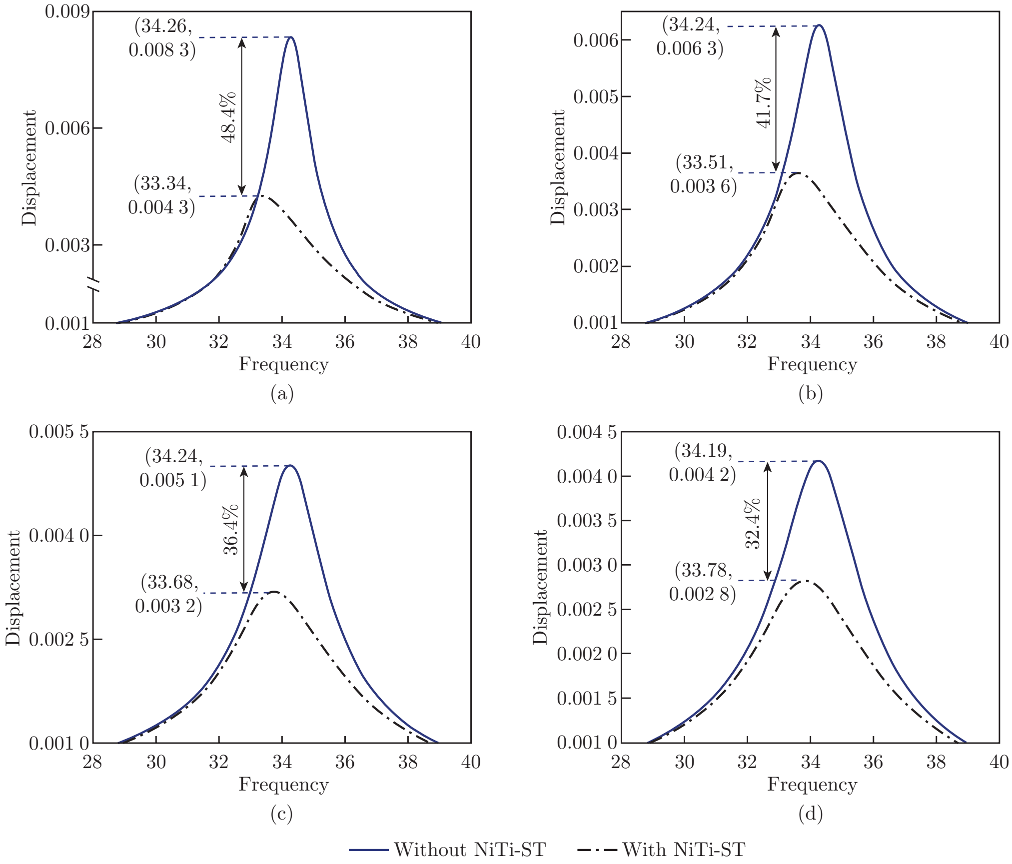

Fig. 9 Displacement responses for different fluid velocities: (a) $\gamma = 0.75$; (b) $\gamma = 1.00$; (c) $\gamma = 1.25$; (d) $\gamma = 1.50$, where $\overline{k}_{\mathrm{R}} = 92.7$, and $\overline{x} = 1$ (color online)

$\gamma = 0.75$ to $\gamma = 1.50$, the vibration absorption performance at the main resonance peak is reduced by 48.4% to 32.4%. Hence, the fluid flow is unfavorable for the vibration absorption of the FGM fluid-conveying pipe.

Figure 10 shows the displacement response of the FGM fluid-conveying pipe at the first main resonance peak for different NiTi-ST configurations. The dimensionless natural frequency of the

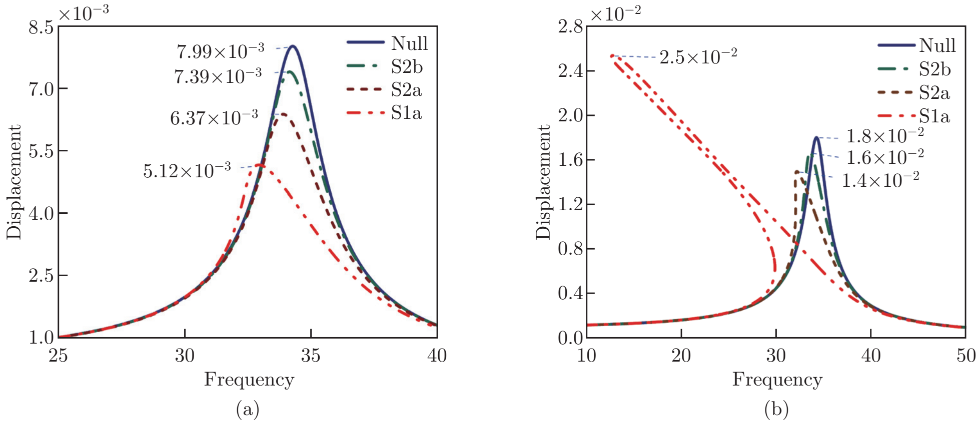

Fig. 10 Vibration absorption for different magnitudes of external excitation with different NiTi-ST configurations: (a) $\overline{f} = 0.80$; (b) $\overline{f} = 1.80$, where $\overline{k}_{\mathrm{R}} = 92.7$, $\gamma = 1.25$, and $\overline{x} = 1$ (color online)

FGM fluid-conveying pipe is 34.25. As shown in Fig. 10(a), the different NiTi-ST configurations successfully reduce the displacement response around the main resonance peak. Overall, the different NiTi-ST configurations have a slightly softening behavior, and the S1a configuration demonstrates an optimizing vibration absorption effect. Nevertheless, the S1a configuration has the best vibration absorption effect for a small excitation amplitude, but its softening behavior is the most evident, and the offset of the main resonance peak is prominent. With the increasing amplitude of the dimensionless external excitation, the sudden changes of the vibration response and resonance frequency of the FGM fluid-conveying pipe with S1a configuration NiTi-ST are shown in Fig. 10(b). The amplitude and natural frequency of the main resonance peak exhibit unacceptable changes. It is necessary to give consideration to the disadvantages when polynomial models are applied.

Figure 11 illustrates the progress of the displacement response with an increase in the external excitation amplitude. The linearized stability theory is used to explore the stability of the response[56]. The red scratch line represents the unstable solution. As illustrated in Fig. 11, when the amplitude of the external excitation increases, the interval of the unstable solution becomes wider. When the amplitude of the dimensionless external excitation increases to $\overline{f} = 1.80$, the displacement response and the resonance frequency change abruptly and significantly, which are much more than those for a small external excitation amplitude.

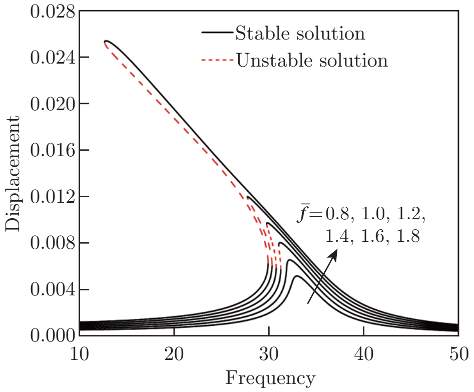

Fig. 11 Vibration response with an increase in the dimensionless external excitation from $\overline{f} = 0.80$ to $\overline{f} = 1.80$ when $\overline{k}_{\mathrm{R}} = 92.7$, $\gamma = 1.25$, and $\overline{x} = 1$ (color online)

Below, the reason for the abrupt changes of the vibration response and resonance frequency is illustrated. When simulating the change of displacement response with external excitation, the vibration response phenomenon named as the CDR is found. As shown in Figs. 12(a) and 12(b), when the external excitation increases from $\overline{f} = 0.80$ to $\overline{f} = 1.10$, a small curve appears above on the right, far from the main resonance peak. In particular, the unstable region is marked red on the CDR, and there is no unstable solution on the main resonance peak. With a further increase in the external excitation, as shown in Figs. 12(c) and 12(d), the CDR curve becomes larger, and the left end of the curve gradually approaches the main resonance peak. In addition, the resonance frequency gets gradually lower as the external excitation increases. Finally, when the external excitation increases to $\overline{f} = 1.70$, the CDR curve begins to merge with the main resonance peak. When the external excitation increases to $\overline{f} = 1.80$, the CDR curve merges completely with the main resonance peak. The merging of the CDR curve and the main resonance peak is observed with changing the external excitation, as shown in Fig. 12(g). This merging illustrates the sudden change of the vibration response and resonance frequency. After the merging of the CDR curve and the main resonance peak, the amplitude of the displacement

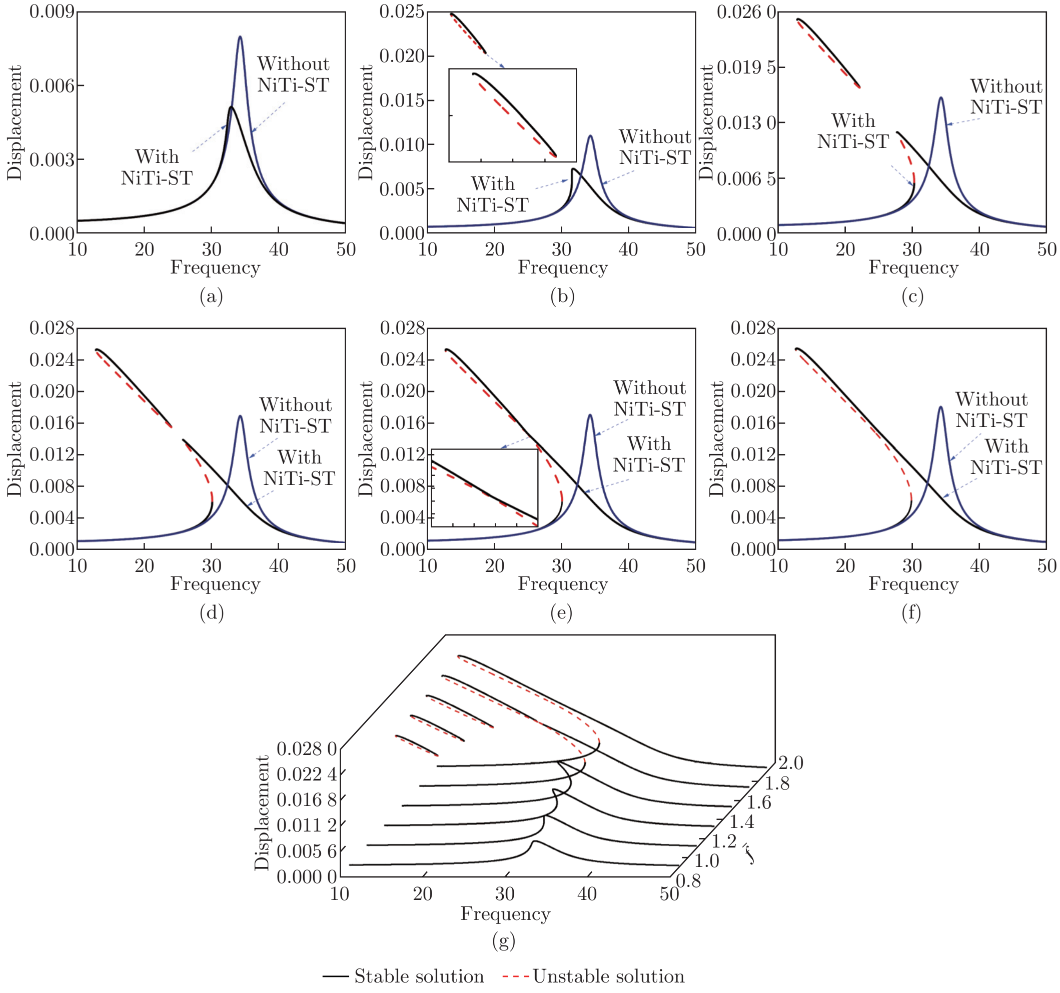

Fig. 12 CDR curves for different dimensionless external excitations: (a) $\overline{f} = 0.80$; (b) $\overline{f} = 1.10$; (c) $\overline{f} = 1.60$; (d) $\overline{f} = 1.69$; (e) $\overline{f} = 1.70$; (f) $\overline{f} = 1.80$, where $\overline{k}_{\mathrm{R}} = 92.7$, $\gamma = 1.25$, and $\overline{x} = 1$. (g) Displacement changing with $\overline{f}$ (color online)

response changes abruptly to 0.025, and the resonance frequency shifts to 12.6. Significantly, with an increment in the external excitation, the CDR curve appears separately before merging with the main resonance peak. The sudden change of the vibration response and resonance frequency relates to the appearance of the CDR curve. This curve has a negative impact on vibration absorption, and the CDR curve will give unsatisfactory responses under large external excitation. It is necessary to give consideration to the possible disadvantage of the CDR curve.

To avoid the unfavorable effect on vibration absorption, Figs. 13(a) and 13(b) illustrate the displacement via the resonance frequency with various values of the parameter $\overline{r}_{12}$ while ensuring reasonable degree of fitting. Figure 13(a) shows that the main resonance peak recovers by decreasing $\overline{r}_{12}$ value, and the region of the unstable solution on the main resonance peak becomes smaller. The NiTi-ST can still provide reasonable vibration absorption. Figure 13(b) illustrates the effect of the parameter $\overline{r}_{12}$ on the CDR curve. As shown in this figure, as the parameter $\overline{r}_{12}$ gets even smaller, the CDR curve shrinks and gradually separates from the main resonance peak. Eventually, the CDR curve disappears while the nonlinear damping coefficient continues to decrease. Based on the discussion above, the effect of damping coefficients on the vibration absorption is complicated in the polynomial model, and the CDR curve can be avoided by changing $\overline{r}_{12}$.

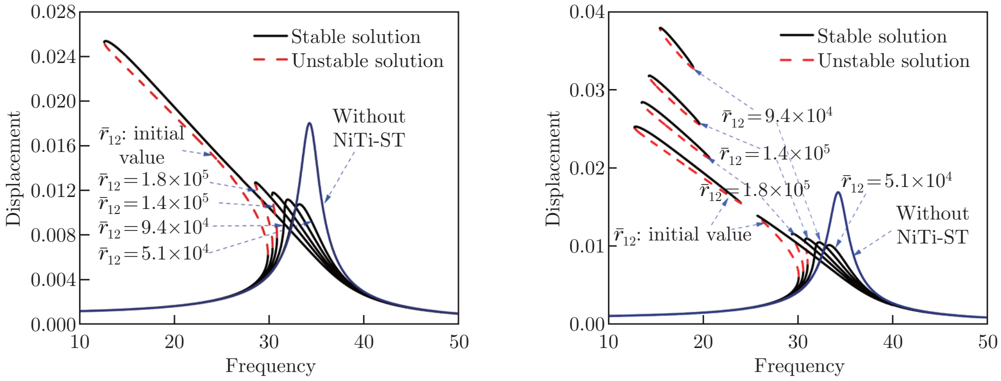

(a) (b)

Fig. 13 Displacements of the main resonance peaks for different values of $\overline{r}_{12}$ when $\overline{k}_{\mathrm{R}} = 92.7$, $\gamma = 1.25$, and $\overline{x} = 1$: (a) $\overline{f} = 1.80$; (b) $\overline{f} = 1.69$ (color online)

Figure 14 shows the effects of the stiffness coefficient and linear damping on vibration absorption. Figure 14(a) shows that the main resonance peak does not change significantly with change of the parameter $\overline{k}_3$. As shown in Fig. 14(b), the vibration absorption ability of $\overline{c}_1$ is also studied. The polynomial model contains many damping-related terms, where $\overline{c}_1$ is the linear damping term. The ability of vibration absorption is enhanced with the increase in $\overline{c}_1$ and the resonance frequency keeping invariable. Based on the above analysis, the linear damping term $\overline{c}_1$ is found to have a major effect on vibration absorption. The stiffness term, by contrast, has no significant effect on vibration absorption.

5 Conclusions

This paper investigates the vibration absorption of an FGM fluid-conveying pipe coupled with NiTi-ST. The restoring and damping forces are determined by a polynomial model. The governing function of the system is obtained based on the Hamilton theory. The governing function is discretized by the GTM. The HBM is used to analyze the vibration response. The effects of the NiTi-ST parameters and the fluid velocity on the absorption performance are investigated. According to the analytical solution, NiTi-ST can absorb the vibration of the

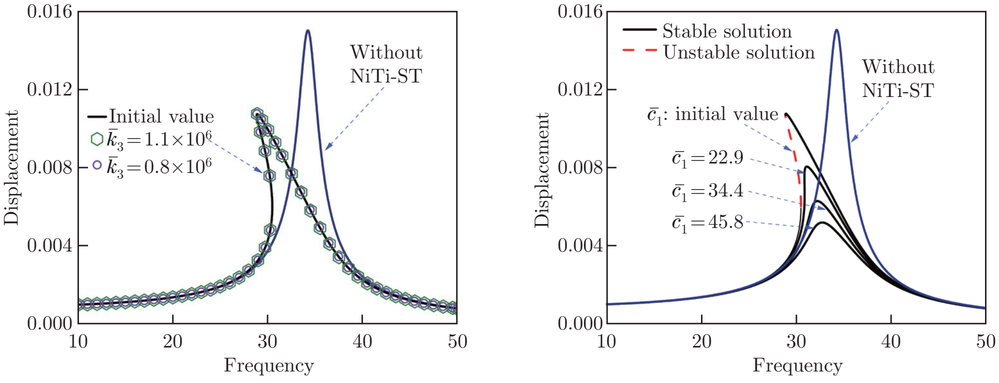

(a)

(b)

Fig. 14 Displacements of the main resonance peaks for different values of (a) $\overline{k}_3$ and (b) $\overline{c}_1$, where $\overline{k}_{\mathrm{R}} = 92.7$, $\gamma = 1.25$, $\overline{x} = 1$, and $\overline{f} = 1.50$ (color online)

system under harmonic excitations. The conclusions are listed as follows.

(I) NiTi-ST can successfully control the vibration response along the FGM fluid-conveying pipe. However, increasing the fluid velocity may affect the vibration absorption.

(II) The S1a configuration has the best vibration absorption, but the softening behavior is the most obvious.

(III) The sudden change of the vibration response and resonance frequency of the fluid-conveying pipe is due to the appearance of the CDR. With the increment in external excitation, the CDR curve gradually approaches the resonance peak and finally merges with the main resonance peak.

(IV) The effects of the damping coefficients of NiTi-ST on the vibration absorption in the polynomial model are complicated. The linear damping coefficient has a major effect on the vibration absorption. The nonlinear damping coefficient is a significant factor affecting the CDR. The occurrence of the CDR can be avoided with a reasonable nonlinear damping coefficient. The stiffness coefficient has no significant effects on the vibration absorption.

Conflict of interest Liqun CHEN is an editorial board member for *Applied Mathematics and Mechanics* (*English Edition*) and was not involved in the editorial review or the decision to publish this article. The authors declare no conflict of interest.

References

[1] PAÏDOUSSIS, M. P. The canonical problem of the fluid-conveying pipe and radiation of the knowledge gained to other dynamics problems across applied mechanics. *Journal of Sound and Vibration*, **310**, 462–492 (2008)

[2] LI, W. C., VAZIRI, V., APHALE, S. S., DONG, S., and WIERCIGROCH, M. Dynamics and frequency and voltage control of downhole oil pumping system. *Mechanical Systems and Signal Processing*, **139**, 106562 (2020)

[3] PAÏDOUSSIS, M. P. and ISSID, N. T. Dynamic stability of pipes conveying fluid. *Journal of Sound and Vibration*, **33**, 267–294 (1974)

[4] PAÏDOUSSIS, M. P. and LI, G. X. Pipe conveying fluid: a dynamical model problem. *Journal of Fluids and Structure*, **7**, 137–204 (1993)

[5] PAÏDOUSSIS, M. P. Some unresolved issues in fluid-structure interactions. *Journal of Fluids and Structures*, **20**, 871–890 (2005)

[6] PENG, G., XIONG, Y., GAO, Y., LIU, L., WANG, M., and ZHANG, Z. Nonlinear dynamics of a simply supported fluid-conveying pipe subjected to motion-limiting constraints: two-dimensional analysis. *Journal of Sound and Vibration*, **435**, 192–204 (2018)

[7] TAN, X., MAO, X. Y., DING, H., and CHEN, L. Q. Vibration around non-trivial equilibrium of a supercritical Timoshenko pipe conveying fluid. *Journal of Sound and Vibration*, **428**, 104–118 (2018)

[8] LU, Z. Q., ZHANG, K. K., DING, H., and CHEN, L. Q. Internal resonance and stress distribution of pipes conveying fluid in supercritical regime. *International Journal of Mechanical Sciences*, **186**, 105900 (2020)

[9] IBRAHIM, R. A. Overview of mechanics of pipes conveying fluid. *Journal of Pressure Vessel Technology*, **132**, 034001 (2010)

[10] TAN, X., DING, H., and CHEN, L. Q. Nonlinear frequencies and forced responses of pipes conveying fluid via a coupled Timoshenko model. *Journal of Sound and Vibration*, **455**, 241–255 (2019)

[11] MIYAMOTO, Y., NIINO, M., and KOIZUMI, M. FGM research programs in Japan — from structural to functional uses. *Functionally Graded Materials*, **1996**, 1–8 (1997)

[12] KIEBACK, B., NEUBRAND, A., and RIEDEL, H. Processing techniques for functionally graded materials. *Materials Science and Engineering*: *A*, **362**, 81–106 (2003)

[13] SU, Z., JIN, G., and YE, T. Three-dimensional vibration analysis of thick functionally graded conical, cylindrical shell and annular plate structures with arbitrary elastic restraints. *Composite Structures*, **118**, 432–447 (2014)

[14] SHEN, H., PAÏDOUSSIS, M. P., WEN, J., YU, D., and WEN, X. The beam-mode stability of periodic functionally-graded-material shells conveying fluid. *Journal of Sound and Vibration*, **333**, 2735–2749 (2014)

[15] DENG, J., LIU, Y., ZHANG, Z., and LIU, W. Dynamic behaviors of multi-span viscoelastic functionally graded material pipe conveying fluid. *Proceedings of the Institution of Mechanical Engineers*, *Part C*: *Journal of Mechanical Engineering Science*, **231**, 3181–3192 (2016)

[16] WANG, Z. M. and LIU, Y. Z. Transverse vibration of pipe conveying fluid made of functionally graded materials using a symplectic method. *Nuclear Engineering and Design*, **298**, 149–159 (2016)

[17] LU, Z. Q., ZHANG, K. K., DING, H., and CHEN, L. Q. Nonlinear vibration effects on the fatigue life of fluid-conveying pipes composed of axially functionally graded materials. *Nonlinear Dynamics*, **100**, 1091–1104 (2020)

[18] SU, Z., INABA, K., KARMAKAR, A., and DAS, A. Analytical and numerical study of vibration and transient heat conduction in a functionally graded pipe. *Journal of Advanced Mechanical Design*, *Systems*, *and Manufacturing*, **15**, 0054 (2021)

[19] TONG, G. J., LIU, Y. S., LIU, H. C., and DAI, J. Y. Thermoelastic vibration analysis of micro-scale functionally graded material fluid-conveying pipes in elastic medium. *Journal of Central South University*, **26**, 2785–2796 (2019)

[20] SALEH, B. I. and AHMED, M. H. Development of functionally graded tubes based on pure Al/Al_2O_3 metal matrix composites manufactured by centrifugal casting for automotive applications. *Metals and Materials International*, **26**, 1430–1440 (2019)

[21] ZHU, B., XU, Q., LI, M., and LI, Y. Nonlinear free and forced vibrations of porous functionally graded pipes conveying fluid and resting on nonlinear elastic foundation. *Composite Structures*, **252**, 112672 (2020)

[22] DING, H., JI, J., and CHEN, L. Q. Nonlinear vibration isolation for fluid-conveying pipes using quasi-zero stiffness characteristics. *Mechanical Systems and Signal Processing*, **121**, 675–688 (2019)

[23] DING, H. and CHEN, L. Q. Designs, analysis, and applications of nonlinear energy sinks. *Nonlinear Dynamics*, **100**, 3061–3107 (2020)

[24] WANG, G. X., DING, H., and CHEN, L. Q. Performance evaluation and design criterion of a nonlinear energy sink. *Mechanical Systems and Signal Processing*, **169**, 108770 (2022)

[25] WANG, G. X. and DING, H. Mass design of nonlinear energy sinks. *Engineering Structures*, **250**, 113438 (2022)

[26] GUO, H., YANG, T., CHEN, Y., and CHEN, L. Q. Singularity analysis on vibration reduction of a nonlinear energy sink system. *Mechanical Systems and Signal Processing*, **173**, 109074 (2022)

[27] GENG, X. F. and DING, H. Two-modal resonance control with an encapsulated nonlinear energy sink. *Journal of Sound and Vibration*, **520**, 116667 (2022)

[28] ZHANG, Y. W., WANG, C., YUAN, B., and FANG, B. Integration of geometrical and material nonlinear energy sink with piezoelectric material energy harvester. *Shock and Vibration*, **2017**, 1987456 (2017)

[29] MA, X. and ZHOU, S. A review of flow-induced vibration energy harvesters. *Energy Conversion and Management*, **254**, 115223 (2022)

[30] ZHOU, S., LALLART, M., and ERTURK, A. Multistable vibration energy harvesters: principle, progress, and perspectives. *Journal of Sound and Vibration*, **528**, 116886 (2022)

[31] HUANG, D., ZHOU, S., LI, R., and YURCHENKO, D. On the analysis of the tristable vibration isolation system with delayed feedback control under parametric excitation. *Mechanical Systems and Signal Processing*, **164**, 108207 (2022)

[32] ZHANG, Y. W., ZHANG, Z., CHEN, L. Q., YANG, T. Z., FANG, B., and ZANG, J. Impulse-induced vibration suppression of an axially moving beam with parallel nonlinear energy sinks. *Nonlinear Dynamics*, **82**, 61–71 (2015)

[33] NILI AHMADABADI, Z. and KHADEM, S. E. Nonlinear vibration control and energy harvesting of a beam using a nonlinear energy sink and a piezoelectric device. *Journal of Sound and Vibration*, **333**, 4444–4457 (2014)

[34] ZHANG, Y. W., ZHANG, H., HOU, S., XU, K. F., and CHEN, L. Q. Vibration suppression of composite laminated plate with nonlinear energy sink. *Acta Astronautica*, **123**, 109–115 (2016)

[35] MAMAGHANI, A. E., KHADEM, S. E., and BAB, S. Vibration control of a pipe conveying fluid under external periodic excitation using a nonlinear energy sink. *Nonlinear Dynamics*, **86**, 1761–1795 (2016)

[36] PAIVA, A. and SAVI, M. A. An overview of constitutive models for shape memory alloys. *Mathematical Problems in Engineering*, **2006**, 1–30 (2006)

[37] OZBULUT, O. E., HURLEBAUS, S., and DESROCHES, R. Seismic response control using shape memory alloys: a review. *Journal of Intelligent Material Systems and Structures*, **22**, 1531–1549 (2011)

[38] LESTER, B. T., BAXEVANIS, T., CHEMISKY, Y., and LAGOUDAS, D. C. Review and perspectives: shape memory alloy composite systems. *Acta Mechanica*, **226**, 3907–3960 (2015)

[39] MANI, Y. and SENTHILKUMAR, M. Shape memory alloy-based adaptive-passive dynamic vibration absorber for vibration control in piping applications. *Journal of Vibration and Control*, **21**, 1838–1847 (2013)

[40] BELHAQ, M., CARBONI, B., and LACARBONARA, W. A new vibration absorber based on the hysteresis of multi-configuration NiTiNOL-steel wire ropes assemblies. *MATEC Web of Conferences*, **16**, 01004 (2014)

[41] CARBONI, B., MANCINI, C., and LACARBONARA, W. Hysteretic beam model for steel wire ropes hysteresis identification. *Springer Proceedings in Physics*, **168**, 261–282 (2015)

[42] CARBONI, B., LACARBONARA, W., and AURICCHIO, F. Hysteresis of multiconfiguration assemblies of nitinol and steel strands: experiments and phenomenological identification. *Journal of Engineering Mechanics*, **141**, 04014135 (2015)

[43] CARBONI, B. and LACARBONARA, W. Nonlinear dynamic characterization of a new hysteretic device: experiments and computations. *Nonlinear Dynamics*, **83**, 23–39 (2015)

[44] BREWICK, P. T., MASRI, S. F., CARBONI, B., and LACARBONARA, W. Data-based nonlinear identification and constitutive modeling of hysteresis in nitinol and steel strands. *Journal of Engineering Mechanics*, **142**, 04016107 (2016)

[45] CARBONI, B., LACARBONARA, W., BREWICK, P. T., and MASRI, S. F. Dynamical response identification of a class of nonlinear hysteretic systems. *Journal of Intelligent Material Systems and Structures*, **29**, 2795–2810 (2018)

[46] BREWICK, P. T., MASRI, S. F., CARBONI, B., and LACARBONARA, W. Enabling reduced-order data-driven nonlinear identification and modeling through naive elastic net regularization. *International Journal of Non-Linear Mechanics*, **94**, 46–58 (2017)

[47] LIU, Y., MOJAHED, A., BERGMAN, L. A., and VAKAKIS, A. F. A new way to introduce geometrically nonlinear stiffness and damping with an application to vibration suppression. *Nonlinear Dynamics*, **96**, 1819–1845 (2019)

[48] ZANG, J. and ZHANG, Y. W. Responses and bifurcations of a structure with a lever-type nonlinear energy sink. *Nonlinear Dynamics*, **98**, 889–906 (2019)

[49] HABIB, G., CIRILLO, G. I., and KERSCHEN, G. Uncovering detachedresonance curves in single-degree-of-freedom. *Procedia Engineering*, **199**, 649–656 (2017)

[50] CHEN, J. E., HE, W., ZHANG, W., YAO, M. H., LIU, J., and SUN, M. Vibration suppression and higher branch responses of beam with parallel nonlinear energy sinks. *Nonlinear Dynamics*, **91**, 885–904 (2017)

[51] ZANG, J., YUAN, T. C., LU, Z. Q., ZHANG, Y. W., DING, H., and CHEN, L. Q. A lever-type nonlinear energy sink. *Journal of Sound and Vibration*, **437**, 119–134 (2018)

[52] ZANG, J., CAO, R. Q., FANG, B., and ZHANG, Y. W. A vibratory energy harvesting absorber using integration of a lever-enhanced nonlinear energy sink and a levitation magnetoelectric energy harvester. *Journal of Sound and Vibration*, **484**, 115534 (2020)

[53] ZANG, J., CAO, R. Q., ZHANG, Y. W., FANG, B., and CHEN, L. Q. A lever-enhanced nonlinear energy sink absorber harvesting vibratory energy via giant magnetostrictive-piezoelectricity. *Communications in Nonlinear Science and Numerical Simulation*, **95**, 105620 (2021)

[54] ZANG, J., CAO, R. Q., and ZHANG, Y. W. Steady-state response of a viscoelastic beam with asymmetric elastic supports coupled to a lever-type nonlinear energy sink. *Nonlinear Dynamics*, **105**, 1327–1341 (2021)

[55] ZHENG, L. H., ZHANG, Y. W., DING, H., and CHEN, L. Q. Nonlinear vibration suppression of composite laminated beam embedded with NiTiNOL-steel wire ropes. *Nonlinear Dynamics*, **103**, 2391–2407 (2021)

[56] ZANG, J. and CHEN, L. Q. Complex dynamics of a harmonically excited structure coupled with a nonlinear energy sink. *Acta Mechanica Sinica*, **33**, 801–822 (2017)